Simulations of Free Shear Layers Using a Compressible $k-\epsilon$ Model

S.T. Yu*
Sverdrup Technology, Inc.,
NASA Lewis Research Group
Brook Park, OH 44142

C.T. Chang† and C.J. Marek‡
NASA Lewis Research Center
Cleveland, Ohio 44135

ABSTRACT

A two-dimensional, compressible Navier-Stokes equations with a $k-\epsilon$ turbulence model are solved numerically to simulate the flows of compressible free shear layers. The appropriate form of k and ϵ equations for compressible flows are discussed. Sarkar's modelling is adopted to simulate the compressibility effects in the k and ϵ equations. The numerical results show that the the spreading rate of the shear layers decreases with increasing convective Mach number. In addition, favorable comparison was found between the calculated results and Goebel and Dutton's experimental data.

INTRODUCTION

Recent national interest in trans-atmospheric vehicle has rekindled the hypersonic research. For this vehicle, a supersonic combustion ramjet (scramjet) engine was proposed to provide the power. Inside this scramjet engine, compressible mixing layers are important phenomena. The performance of the engine will depend on the supersonic mixing and the flame holding of shear layers.

The behavior of incompressible mixing layers has been studied extensively. However, additional study is required to understand the compressibility effects of free shear layers at high speeds. Figure 1 shows a sketch of a typical free shear layer. Two streams at different temperatures, densities, and Mach numbers merge together to form a free shear layer. Various combinations of flow conditions of high-speed streams and low-speed streams allow for the systematic study of compressible shear layers. In this paper, we report the incorporation of a $k-\epsilon$ model with compressibility effects to a two-dimensional flow equations solver for the simulation of compressible shear layers. First, we point out the derivation procedure of the compressible k and ϵ equations. Unlike the procedure in the incompressible equations, both Favre and Reynolds averaging procedures[1] are performed in deriving the flow and turbulence equations. Particularly, the additional terms in the Navier-Stokes equations due to the averaging procedure are illustrated. These terms are often omitted in CFD practices. The k and ϵ equations are presented in vector form for the convenience of illustrating the numerical method.

The lower-upper (LU) scheme developed by Yoon and Jameson[2] is adopted in this work. This method has proven very efficient for large systems of equations.[3] For completeness, a brief account of the numerical method is presented in this paper. The newly developed solver then is applied to simulate compressible free shear layers with five different convective Mach numbers from 0.05 to 1.48. One of five test conditions is a replica of that reported by Goebel and Dutton.[4] The most important feature of the compressible free shear layers one want to demonstrate in the calculations is the decrease of the shear layer thickness with increasing Mach number.[5] Favorable comparison were found between the experimental data and the calculated results.

THEORETICAL MODEL

In deriving the compressible flow equations of fully turbulent flows, all the flow properties are Favre averaged (mass weighted averaged) except the density, ρ, and pressure, p. The definition of the Favre average is

$$\tilde{\phi} = \overline{\phi\rho}/\overline{\rho}. \qquad (1)$$

* Research Engineer, Member AIAA.
† Aerospace Engineer, Member AIAA.
‡ Senior Research Scientist.

where ϕ is any flow property. Thus flow variables are decomposed in the following fashion,

$$\phi = \tilde{\phi} + \phi". \tag{2}$$

On the other hand, conventional Reynolds' average are used for the pressure and the density. According to the definition of Favre averaging, the following relations exist:

$$\begin{aligned} \overline{\phi"} &= -\frac{\overline{\rho'\phi'}}{\overline{\rho}}, \\ \overline{\rho\phi"} &= 0, \\ \overline{\phi'} &= 0. \end{aligned} \tag{3}$$

In doing so, all the terms associated with the density fluctuation, e.g., $\overline{\rho'u'}$, in the Reynolds' averaged equations were eliminated in the Favre's averaged equations. The resulting flow equations are much simpler compared to the equations derived by the Reynolds averaging procedures.

Written in a strong conservative form, the turbulent, compressible, flow equations can be expressed as follows:

$$\frac{\partial \mathbf{Q}}{\partial t} + \frac{\partial}{\partial x}(\mathbf{E} - \mathbf{E}_v) + \frac{\partial}{\partial y}(\mathbf{F} - \mathbf{F}_v) = \mathbf{H}. \tag{4}$$

Here x and y are Cartesian coordinates, $\mathbf{Q}$ is the dependent variable, $\mathbf{E}$ and $\mathbf{F}$ are the convective flux vectors and $\mathbf{E}_v$ and $\mathbf{F}_v$ are the viscous flux vectors. The equations are similar to the laminar equations. However, all variables in the equations are the averaged variables, and the transport properties are the effective, i.e., laminar plus turbulent, properties. Here, we want to point out that the viscosity multiplied by the dilatational terms in the normal stresses is still the laminar viscosity as illustrated in the following relations:

$$\begin{aligned} \tau_{xx} &= 2(\mu + \mu_t)\frac{\partial \tilde{u}}{\partial x} - \frac{2}{3}\mu\left(\frac{\partial \tilde{u}}{\partial x} + \frac{\partial \tilde{v}}{\partial y}\right), \\ \tau_{yy} &= 2(\mu + \mu_t)\frac{\partial \tilde{v}}{\partial y} - \frac{2}{3}\mu\left(\frac{\partial \tilde{u}}{\partial x} + \frac{\partial \tilde{v}}{\partial y}\right). \end{aligned} \tag{5}$$

The vector $\mathbf{H}$ on the right hand side of the flow equations, Eq. 4, represents the additional terms introduced by the averaging procedure. The vector $\mathbf{H}$ can be expressed as

$$\mathbf{H} = \begin{pmatrix} 0 \\ -\frac{2}{3}\frac{\partial \overline{\rho}k}{\partial x} \\ -\frac{2}{3}\frac{\partial \overline{\rho}k}{\partial y} \\ \frac{\partial}{\partial x}\left[(\mu + \frac{\mu_t}{\sigma_k})\frac{\partial k}{\partial x}\right] + \frac{\partial}{\partial y}\left[(\mu + \frac{\mu_t}{\sigma_k})\frac{\partial k}{\partial y}\right] \\ +2\tilde{u}\frac{\partial}{\partial x}(\overline{\rho}k) + 2\tilde{v}\frac{\partial}{\partial y}(\overline{\rho}k) + G \end{pmatrix}. \tag{6}$$

where k is the turbulent kinetic energy and is defined as

$$k = \frac{1}{2\overline{\rho}}\overline{\rho(u"u" + v"v")}, \tag{7}$$

G is the generation of the turbulent kinetic energy and is defined in the following section.

The equations of turbulent kinetic energy, k, and energy dissipation rate, ϵ, are derived by the manipulation of the flow equations and the averaging procedure. The derived equations of k and ϵ can not be solved directly due to the closure problem. Modelling of certain terms in the equations is necessary to make the governing equations well posed. The details of the modelling is beyond the scope of this work. Here, only the final form of the equations are presented. The k and ϵ equations in the Cartesian coordinate system can be cast into the vector form: .

$$\frac{\partial \mathbf{Q}_{ke}}{\partial t} + \frac{\partial \mathbf{E}_{ke}}{\partial x} + \frac{\partial \mathbf{F}_{ke}}{\partial y} = \frac{\partial \mathbf{E}_{vke}}{\partial x} + \frac{\partial \mathbf{F}_{vke}}{\partial y} + \mathbf{S}, \tag{8}$$

where

$$\begin{aligned} \mathbf{Q}_{ke} &= \begin{pmatrix} \overline{\rho}k \\ \overline{\rho}\epsilon \end{pmatrix}, \\ \mathbf{E}_{ke} &= \begin{pmatrix} \overline{\rho}\tilde{u}k \\ \overline{\rho}\tilde{u}\epsilon \end{pmatrix}, \\ \mathbf{F}_{ke} &= \begin{pmatrix} \overline{\rho}\tilde{v}k \\ \overline{\rho}\tilde{v}\epsilon \end{pmatrix}, \\ \mathbf{E}_{vke} &= \begin{pmatrix} (\mu + \frac{\mu_t}{\sigma_k})\frac{\partial k}{\partial x} \\ (\mu + \frac{\mu_t}{\sigma_\epsilon})\frac{\partial \epsilon}{\partial x} \end{pmatrix}, \\ \mathbf{F}_{vke} &= \begin{pmatrix} (\mu + \frac{\mu_t}{\sigma_k})\frac{\partial k}{\partial y} \\ (\mu + \frac{\mu_t}{\sigma_\epsilon})\frac{\partial \epsilon}{\partial y} \end{pmatrix}, \\ \mathbf{S} &= \begin{pmatrix} G - \overline{\rho}\epsilon(1 + \alpha M_t^2) \\ (C_1 G - C_2\overline{\rho}\epsilon)\frac{\epsilon}{k} \end{pmatrix}, \end{aligned} \tag{9}$$

where G is the generation term of the turbulent kinetic energy and can be expressed as:

$$G = \mu_t\left[\frac{1}{2}\left(\frac{\partial \tilde{u}_i}{\partial x_j} + \frac{\partial \tilde{u}_j}{\partial x_i}\right) - \frac{2}{3}\frac{\partial \tilde{u}_k}{\partial x_k}\right] - \frac{2}{3}\overline{\rho}k\frac{\partial \tilde{u}_k}{\partial x_k} \tag{10}$$

where the subscripts i, j, and k follows the convention of Cartesian tensor.

The eddy viscosity μ_t is derived in terms of appropriate length and velocity scales. For the $k - \epsilon$ turbulence model, the length scale and the velocity scale of turbulent fluctuations are taken as

$$\begin{aligned} \ell &\approx \frac{k^{3/2}}{\epsilon}, \\ u"_i &\approx k^{1/2}. \end{aligned} \tag{11}$$

These relations allow the eddy viscosity, μ_t, to be modelled as:

$$\mu_t = C_\mu \overline{\rho} \frac{k^2}{\epsilon}. \tag{12}$$

The constants used in the $k-\epsilon$ model are the standard Jones and Launder's values:[6] $C_\mu = 0.09$, $C_1 = 1.44$, $C_2 = 1.92$, $\sigma_k = 1.0$, and $\sigma_\epsilon = 1.3$. These constants were never altered during the course of this work.

In order to accommodate the compressibility effect, the dissipation term $\overline{\rho}\epsilon$ in the source term of the k equation is multiplied by a correction factor $(1+\alpha M_t^2)$. Here M_t is the local turbulence Mach number defined as $M_t = \sqrt{k}/a$ where a is the local speed of sound. The constant α in the term is taken as unity. This model is developed by Sarkar et al.[7] The physical meaning of the term is that for high turbulence Mach number (M_t) flows, the dissipation of the turbulence kinetic energy is enhanced by a factor of αM_t^2. For free shear layers at high convective Mach number, the turbulence intensity is greatly reduced due to compressibility.

In calculating the turbulent free shear layers, the inlet boundary conditions for mean velocities and temperature are specified based on the hyperbolic tangent profile with specified initial shear layer thickness. The hyperbolic tangent profile is an approximation of the self-similar solution for fully developed turbulent free shear layers. The inlet transverse velocities are set to be zero. The turbulent kinetic energy and dissipation are specified according to the local equilibrium assumption and a algebraic turbulence model:[8]

$$\mu_t = \overline{\rho} l_m^2 \frac{\partial \tilde{u}}{\partial y} \tag{13}$$

where $l_m = 0.125b$ and the shear layer thickness, b, is based on the distance between the two transverse locations where $\tilde{u} = \tilde{u}_1 - 0.1\Delta\tilde{u}$ and $\tilde{u} = \tilde{u}_2 + 0.1\Delta\tilde{u}$. The dissipation can be related to the local length scale which is specified based on the local shear layer thickness:

$$\epsilon = C_\epsilon \frac{k^{\frac{3}{2}}}{b} \tag{14}$$

where $C_\epsilon = 1.23$. Using Eqs. (13) and (14), and the equation for the eddy viscosity, i.e, Eq. (12), k and ϵ can be readily obtained for the upstream boundary conditions.

Numerical Method

The numerical solution of Eqs. (4) and (8) is performed in a general, body-fitted coordinate system, (ξ, η). For the purpose of discussion, we will concentrate on Eq. (4). However, the procedure is equally applicable to Eq. (8). Coordinate transformation of Eq. (4) results in:

$$\frac{\partial \hat{\mathbf{Q}}}{\partial \tau} + \frac{\partial}{\partial \xi}\left(\hat{\mathbf{E}} - \hat{\mathbf{E}}_v\right) + \frac{\partial}{\partial \eta}\left(\hat{\mathbf{F}} - \hat{\mathbf{F}}_v\right) = \hat{\mathbf{H}} \tag{15}$$

where

$$\begin{aligned} \hat{\mathbf{Q}} &= h\mathbf{Q} \\ \hat{\mathbf{E}} &= h(\xi_x \mathbf{E} + \xi_y \mathbf{F}) \\ \hat{\mathbf{F}} &= h(\eta_x \mathbf{E} + \eta_y \mathbf{F}) \\ \hat{\mathbf{E}}_v &= h(\xi_x \mathbf{E}_v + \xi_y \mathbf{F}_v) \\ \hat{\mathbf{F}}_v &= h(\eta_x \mathbf{E}_v + \eta_y \mathbf{F}_v) \\ \hat{\mathbf{H}} &= h\mathbf{H} \end{aligned} \tag{16}$$

in which h is the cell volume.

The transformed equation, Eq. (15), is solved using a time-marching, LU scheme. The LU scheme can be obtained by approximately factorizing the left-hand-side (LHS) of the equation. In time-marching form, the implicit upwind difference scheme of Eq. (15) can be written as

$$\begin{aligned} [\mathbf{I} + \Delta t(D_\xi^+ \hat{\mathbf{A}}^- + D_\eta^+ \hat{\mathbf{B}}^- - \hat{\mathbf{D}} + \\ D_\xi^- \hat{\mathbf{A}}^+ + D_\eta^- \hat{\mathbf{B}}^+)]\Delta\hat{\mathbf{Q}} = \Delta t RHS \end{aligned} \tag{17}$$

In Eq. (17), Δt is the time-step. Backward-difference operators are denoted by D_ξ^- and D_η^-, and forward-difference operators by D_ξ^+ and D_η^+. The flux Jacobians, $\hat{\mathbf{A}}^+$, $\hat{\mathbf{B}}^+$, $\hat{\mathbf{A}}^-$, and $\hat{\mathbf{B}}^-$ are constructed such that the eigenvalues of '+' matrices are nonnegative and those of '−' matrices are nonpositive. The matrix $\hat{\mathbf{D}}$ is the Jacobian matrix of the source term.

The LHS matrix of Eq. (21) is usually too large for direct inversion. An approximate-factorization procedure is implemented which results in the following LU scheme :

$$\begin{aligned} &\left[\mathbf{I} + \Delta t\left(D_\xi^- \hat{\mathbf{A}}^+ + D_\eta^- \hat{\mathbf{B}}^+ - \frac{\hat{\mathbf{A}}^-}{\Delta\xi} - \frac{\hat{\mathbf{B}}^-}{\Delta\eta} - \hat{\mathbf{D}}\right)\right] \\ &\left(\frac{\Delta t}{\Delta\xi}(\hat{\mathbf{A}}^+ - \hat{\mathbf{A}}^-) + \frac{\Delta t}{\Delta\eta}(\hat{\mathbf{B}}^+ - \hat{\mathbf{B}}^-) - \hat{\mathbf{D}}\right)^{-1} \\ &\left[\mathbf{I} + \Delta t\left(D_\xi^+ \hat{\mathbf{A}}^- + D_\eta^+ \hat{\mathbf{B}}^- + \frac{\hat{\mathbf{A}}^+}{\Delta\xi} + \frac{\hat{\mathbf{B}}^+}{\Delta\eta} - \hat{\mathbf{D}}\right)\right]\Delta\hat{\mathbf{Q}} \\ &= \Delta t \mathbf{R} \end{aligned} \tag{18}$$

where the grid spacing in the general coordinate, $\Delta\xi$ and $\Delta\eta$ are usually taken to be one. $\mathbf{R}$ represents the residual of each LU time marching step. In calculating the residual, $\mathbf{R}$, both the inviscid and viscous terms are discretized using the central-difference approach:

$$\mathbf{R} = D_\xi(\hat{\mathbf{E}}_v - \hat{\mathbf{E}}) + D_\eta(\hat{\mathbf{F}}_v - \hat{\mathbf{F}}) + \hat{\mathbf{H}} \tag{19}$$

where D_ξ and D_η are the central difference operators.

Equation (18) is the generic form for the LU scheme. Its derivation can be found in Ref. 3 and will not be repeated here. This LU scheme requires inversion of the matrix,

$$\left[\mathbf{I}+\Delta t\left(\hat{\mathbf{A}}^{+}-\hat{\mathbf{A}}^{-}+\hat{\mathbf{B}}^{+}-\hat{\mathbf{B}}^{-}-\hat{\mathbf{D}}\right)\right] \qquad (20)$$

for the L operator and

$$\left[\mathbf{I}+\Delta t\left(\hat{\mathbf{A}}^{+}-\hat{\mathbf{A}}^{-}+\hat{\mathbf{B}}^{+}-\hat{\mathbf{B}}^{-}-b\hat{f}D\right)\right] \qquad (21)$$

for the U operator.

Up to this point, no definition has been made to the exact form of the split flux Jacobians. Yoon and Jameson[2] proposed that the split flux Jacobians are defined as

$$\begin{aligned}\hat{\mathbf{A}}^{+} &= 0.5(\hat{\mathbf{A}}+\gamma_{\hat{\mathbf{A}}}\mathbf{I})\\ \hat{\mathbf{A}}^{-} &= 0.5(\hat{\mathbf{A}}-\gamma_{\hat{\mathbf{A}}}\mathbf{I})\\ \hat{\mathbf{B}}^{+} &= 0.5(\hat{\mathbf{B}}+\gamma_{\hat{\mathbf{B}}}\mathbf{I})\\ \hat{\mathbf{B}}^{-} &= 0.5(\hat{\mathbf{B}}-\gamma_{\hat{\mathbf{B}}}\mathbf{I})\end{aligned} \qquad (22)$$

where $\gamma_{\hat{\mathbf{A}}}$ and $\gamma_{\hat{\mathbf{B}}}$ are greater than the spectral radii of the associated flux Jacobians :

$$\begin{aligned}\gamma_{\hat{\mathbf{A}}} &\geq \max(|\lambda_{\hat{\mathbf{A}}}|)\\ \gamma_{\hat{\mathbf{B}}} &\geq \max(|\lambda_{\hat{\mathbf{B}}}|)\end{aligned} \qquad (23)$$

The purpose of constructing split flux-Jacobians by Eq. (22) is to make the matrices in Eqs. (20) and (21) diagonal for efficient inversion. Apparently, the eigenvalues of the split flux-Jacobians are not the characteristics speeds of the flow.

In solving the k and ϵ equations, the aforementioned numerical method, i.e., the LU scheme on the left hand side and central differencing on the right hand side, is used. The solution procedure of the whole equation set is decoupled into flow solver and turbulence solver. Thus, the turbulence solver stands alone and can be easily turned on or off. This arrangement does not affect the overall numerical stability due to the fact that the feedback from k and ϵ equations to the flow equations depends on the turbulent transport properties only. Thus, it is more efficient and convenient to separate the solution procedure into two parts.

The source terms of the k and ϵ equations demand special treatment. In linearizing the source terms for the numerical method, the Jacobian matrix is obtained through the derivative of the source terms with respect to the dependent variables, i.e., $\overline{\rho}k$ and $\overline{\rho}\epsilon$. Following the usual practice, the form of the source terms guarantee a 2×2 full matrix for the Jacobian matrix. However, special treatment in deriving the Jacobian matrix is applied in this work to enhance the numerical stability. In the k equation, ϵ has been replaced by $k(\epsilon/k)$ where ϵ/k is treated as a constant. A similar method is also applied to the source term of the ϵ equation. The Jacobian matrix obtained is:

$$\mathbf{D}=\begin{pmatrix}-\frac{\epsilon}{k}(1+\alpha M_t^2) & 0\\ 0 & -C_2\frac{\epsilon}{k}\end{pmatrix} \qquad (27)$$

Note that off-diagonal terms are eliminated and the diagonal terms are always negative. Thus, the implicit part of the source terms of k and ϵ equations behaves like a sink which always stabilize the numerical scheme.

Results and Discussions

Bogdanoff[5] introduced the convective Mach number as a parameter that collapses the growth rate date of plane shear layers. The convective Mach number is defined as

$$M_c=\frac{U_1-U_c}{c_1}=\frac{U_c-U_2}{c_2} \qquad (28)$$

where U_1 and U_2 are the freestream velocities, and c_1 and c_2 are the freestream sound speeds. U_c is the convective velocity of large structures and is defined as

$$U_c=\frac{U_1c_2+U_2c_1}{c_1+c_2} \qquad (29)$$

Table 1 shows the five test conditions of the simulated compressible free shear layers. The range of the convective Mach numbers, M_c, is from 0.05 to 1.48. The last two rows show the spreading rate and the ratio of the compressible spreading rate to incompressible spreading rate in which δ is the shear layer thickness and the superscript $'$ represents the derivative of δ with respect to the streamwise distance. As indicated in the last row of the table, the ratios of the spreading rate of the free shear layers decreases as the convective Mach number increases. The test conditions of Case 3 in the table are the same as in the experiments reported by Goebel and Dutton.[4] In the rest of the section, we will first show the direct comparison between the simulated results and the experimental data for Case 3. Then, detailed numerical solutions of Case 3 in terms of velocity, turbulent kinetic energy, turbulence dissipation rate, Reynolds stress, and eddy viscosity are presented in a coalesced fashion. Finally, the solutions of five cases are compared to each other in the figures of kinetic energy, Reynolds stress, and ratio of spreading rates.

The solutions of Case 3 are examined in detail. Figure 2 shows the development of the free shear layer.

Note that x and y axes are not on a 1:1 ratio for the convenience of illustration. The definition of the shear layer boundaries is the same that of the shear layer thickness. In Fig. 2, the boundaries of the shear layer corresponding to $10 - 90\%$ are drawn. Circles are the experimental data of Dutton et al. The calculated results agree well with the experimental data. After the developing region, the boundary of the shear layer is almost linear. Incidentally, Figs. 3a and 3b show the numerical convergence trends of the flow and $k - \epsilon$ equations. In about 2500 iterations, the residuals drop about 12 orders of magnitude and reach the machine accuracy.

Figure 4 shows the Mach number profile at various axial locations. The velocity gradient in the transverse direction decreases as the flow goes downstream. Figure 5 is the coalesced version of Fig. 4. The nondimensionalized y coordinate defined as $(y - y_c)/\delta$ is used, where y_c is the transverse location at the center of the shear layer, and δ is the shear layer thickness. Note that the upstream boundary condition of velocities is prescribed according to a hyperbolic tangent curve which is an approximation of self-similar solution of free shear layers. According to Fig. 5, this self similarity of velocity profiles never fail as the flow goes downstream.

Figure 6 shows coalesced turbulence kinetic energies at various locations. The turbulence kinetic energy is nondimensionalized by ΔU^2. This figure clearly shows that after the first three stations, i.e., about 150 mm, the turbulence kinetic energy retains self similarity. Thus, the developing region for the turbulence is about 150 mm. Figure 7 shows the turbulence dissipation profiles. As flow goes downstream, the peak values of turbulence dissipation at each stations decrease, and the turbulence dissipation never reach a fully developed condition. However, if the ϵ value is nondimensionalized by $\Delta U^3/\delta$ the coalesced profiles appear as shown in Fig. 7. A similar behavior is observed for the eddy viscosity profiles (Fig. 8). Figure 9 shows the nondimensionalized Reynolds stress profiles. Again, the turbulence Reynolds stress becomes the fully developed at about 150 mm downstream of the splitter plate.

Figure 10 shows the comparison between the predicted fully developed Reynolds stress and the experimental data reported by Dutton et al.[5] The predicted solution underestimated the peak value of the Reynolds stress profile by $6 \sim 8\%$; however, the overall trend of the predicted results is correct. Many factors contribute to the discrepancy between the predicted result and experimental data. Among them, the upstream boundary conditions are simplified in the solution procedure, i.e., no effort was made to simulate two boundary layers merging at the tip of the splitter plate. This could offset the solution in the developing region and shift the fully developed solutions.

Figure 11 shows the comparison of the turbulent kinetic energy between the five cases. Again, the turbulent kinetic energy is normalized by the square of the velocity difference of the two streams. It is clear that the normalized turbulence intensity decreases with increasing convective Mach number. A similar situation is observed in Fig. 12, the normalized Reynolds stress decreases with increasing convective Mach number. Figure 13 shows the distribution of the ratios of spreading rates for the five cases compared to experimental data. The ratio of the spreading rates decreases from about unity to 0.45 as the convective mach number increases from about 0. to 1.45. Both the experimental data and the simulated results show the spreading rate ratio reaches an asymptotic value after the convective mach number exceeds unity. Simular phenomenon can be seen in Figs. 11 and 12. Both figures show that the normalized turbulence kinetic energy and Reynolds stress reach asymptotic values as the convective Mach number increases.

CONCLUDING REMARKS

In this paper, we report the incorporation of a compressible $k - \epsilon$ model with a two-dimensional Navier Stokes solver to study compressible free shear layers. Sarkar's modelling is adopted to simulate the compressibility effects of the k and ϵ equations. The model enhances the turbulence dissipation rate of flows at high speeds. In deriving the governing equations, the Favre averaging procedure for the fully trubulent flow equations is elaborated. The equation sets are presented in the vector form for the convenience of the discussion of the numerical method. Yoon and Jameson's LU scheme is used to solve the equation sets. Details of boundary conditions and the treatment of the source terms of the k and ϵ equations are discussed. Then the program is applied to simulate compressible free shear layers with five different convective Mach numbers. The decrease of the spreading rate of the shear layers with increasing Mach number is observed in the calculated results. Results also show favorable comparison with Goebel and Dutton's experimental data.

REFERENCES

1. Kuo, K.K., 1986 "Principles of Combustion," John Wiely & Sons, p. 412.
2. Yoon, S. and Jameson, A., 1989 "Lower-Upper Implicit Schemes with Multiple Grids for the Euler Equations," *AIAA J.* Vol. 25, No. 7, p. 929.

3. Yu, S.T., Tsai, Y.P., and Shuen, J.S., 1989 "Three-Dimensional Calculation of Supersonic Reacting Flows Using an LU Scheme," AIAA paper 89-0391 (accepted for publications in J. of Compt. Phys.)

4. Goebel, S.G., and Dutton, J.C. 1991 "Experimental Study of Compressible Turbulent Mixing Layers," *AIAA J.* Vol. 29, No. 4, p.538.

5. Bogdanoff, D.W., 1983 "Compressibility Effects in Turbulent Shear Layers," *AIAA J.* Vol. 21, No. 6, p.926.

6. Jones, W.P., and Launder, B.E., 1972 "The Prediction of Laminarization with a Two-Equation Model of Turbulence," *Int. J. Heat Mass Transfer,* Vol. 15, p. 301.

7. Sarkar, S., Erlebacher, G., Hussaini, M.Y., and Kreiss, H.O., 1989 "The Analysis and Modeling of Dilatational Terms in Compressible Turbulence," ICASE Report No. 89-79, NASA Langley Research Center.

8. Burr, R.F. and Dutton, J.C., 1990 "Numerical Modeling of Compressible Reacting Turbulent Shear Layers," AIAA Paper 90-1463.

9. Papamoschou, D. and Roshko, A. 1988 "The Compressible Turbulent Mixing Layer: An Experimental Study," J. Fluid Mech., Vol. 197, p.453.

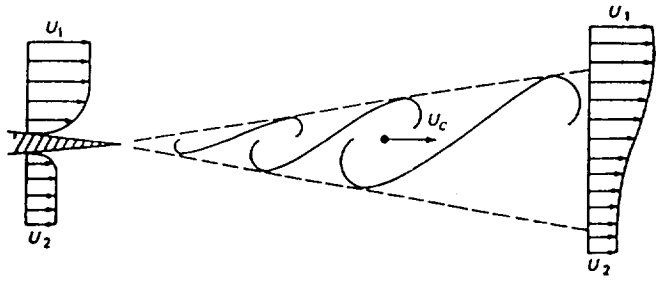

Fig. 1: Schematic of free shear layer.

Table 1: Test conditions of the calculated shear layer.

CASE	1	2	3	4	5
M_1,M_2	1.2, 1.1	2.0, 1.4	1.91, 1.37	2.5, 1.1	6.1, 3.15
M_c	0.05	0.31	0.45	0.70	1.48
U_1,U_2 [m]	419, 384	676, 465	702, 404	865, 380	3461, 1786
T_1,T_2 [K]	300, 300	275, 275	334, 215	295, 295	800, 800
ρ_1,ρ_2 [Kg/m^3]	0.64,0.64	0.7,0.7	0.57,0.89	0.64,0.64	0.24,0.24
P [atm]	0.55	0.55	0.55	0.55	0.55
δ'	0.007	0.021	0.027	0.035	0.024
δ'/δ'_i	1.01	0.7	0.54	0.47	0.40

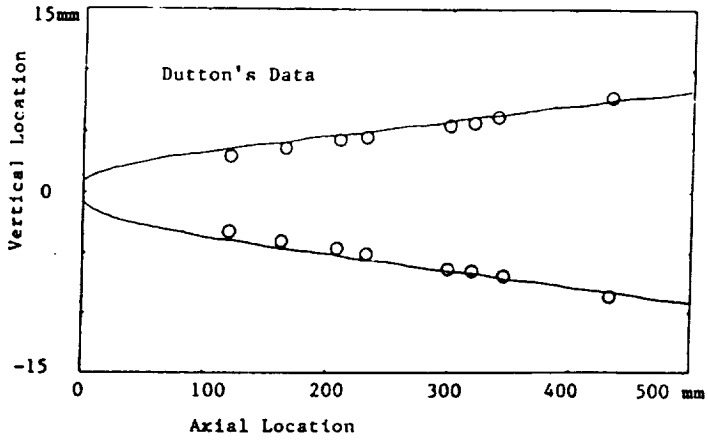

Fig. 2: The boundaries of the free shear layer (10−−90%).

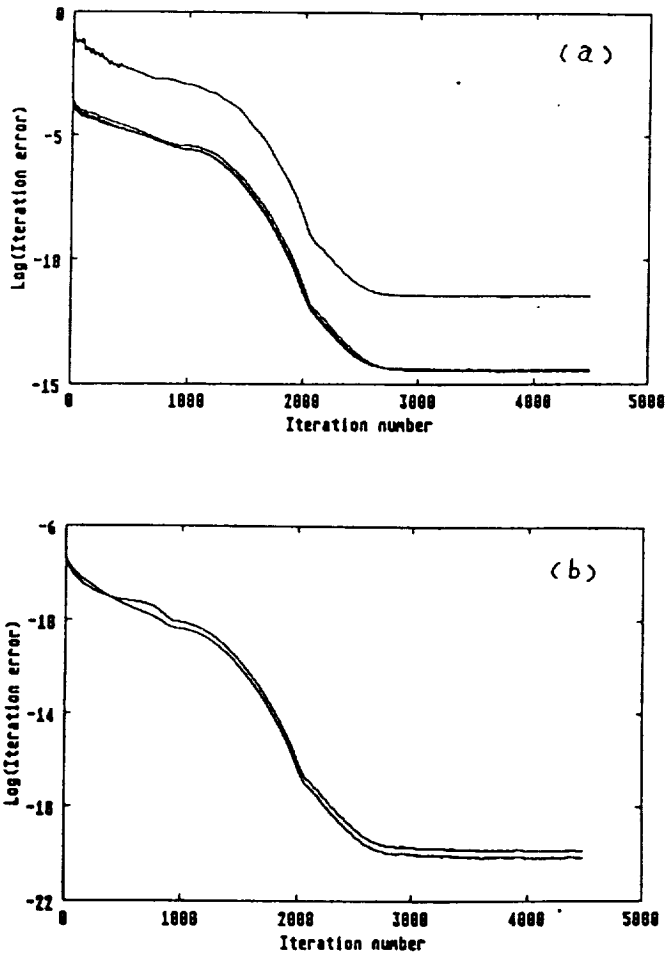

Fig. 3: Convergence trends of the flow and turbulence equations.

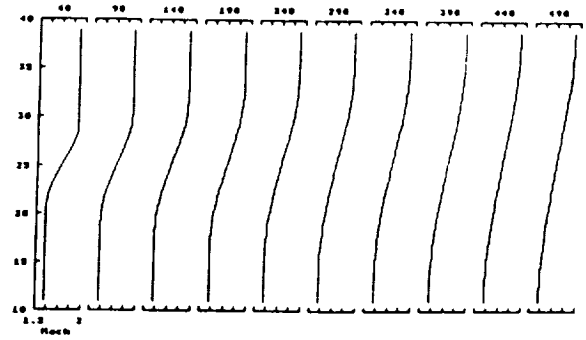

Fig. 4: The velocity profiles of the free shear layer at different axial locations.

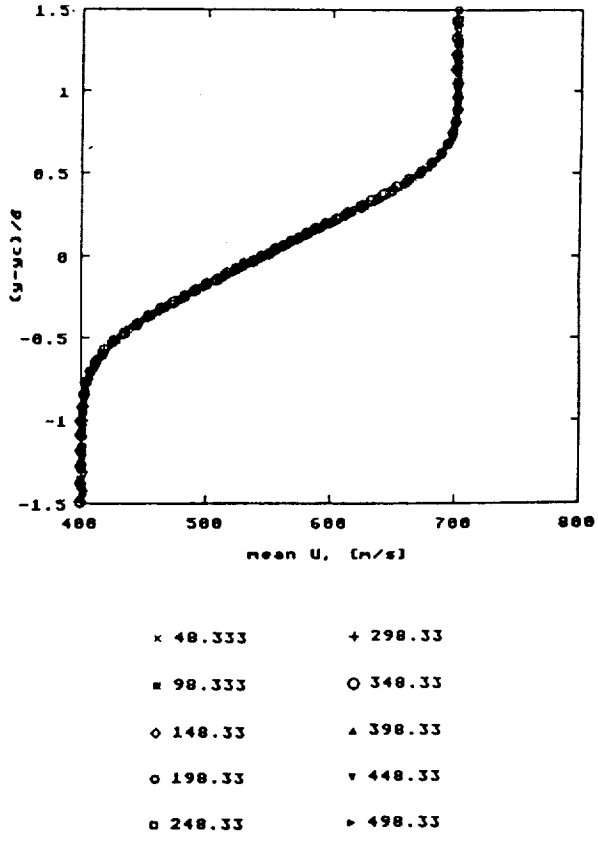

Fig. 5: Coalesced velocity profiles of different axial locations.

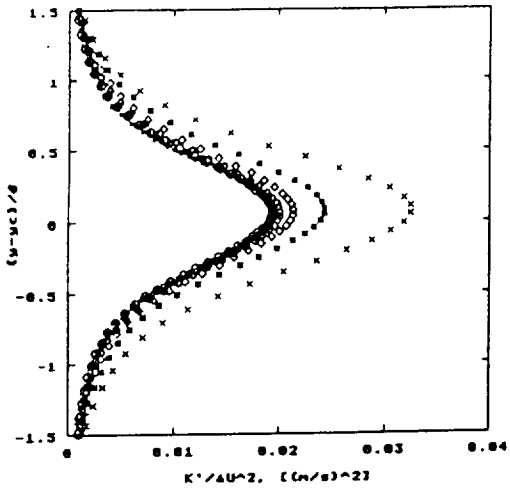

Fig. 6: Coalesced turbulent kinetic energy profiles of different axial locations.

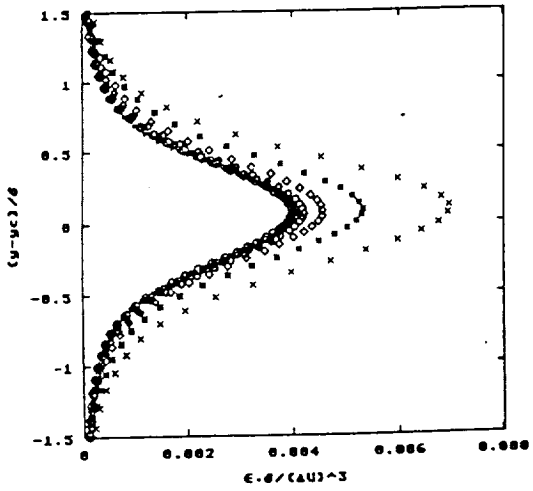

Fig. 7: Coalesced turbulence dissipation profiles of different axial locations.

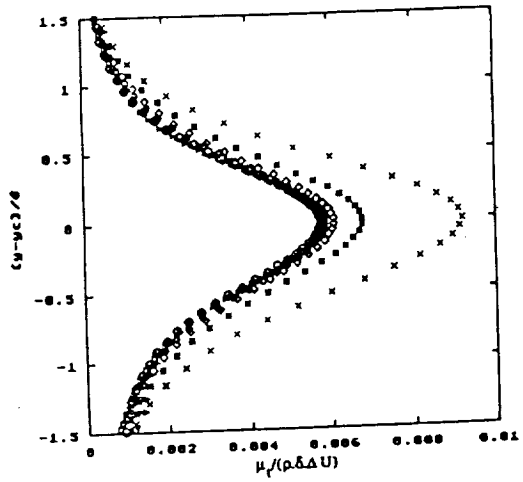

Fig. 8: Coalesced eddy viscosity profiles of different axial locations.

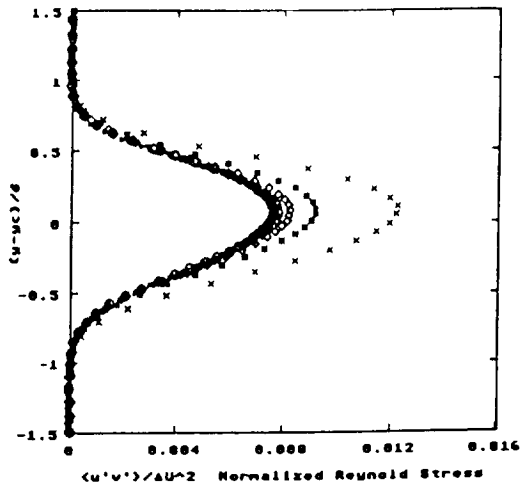

Fig. 9: Coalesced Reynolds stress profiles of different axial locations.

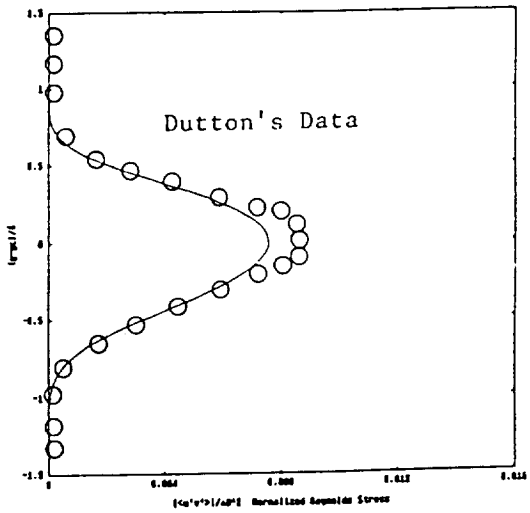

Fig. 10: Comparison of Reynolds stresses between experimental data and predicted results.

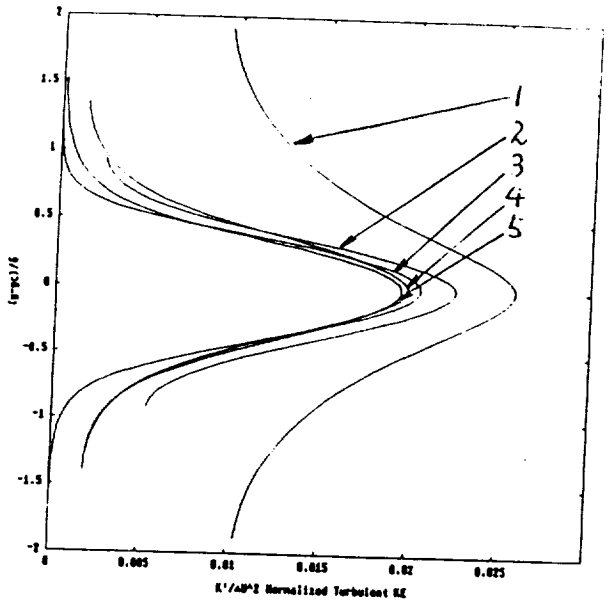

Fig. 11: Comparison of turbulent kinetic energy with five different convective Mach numbers.

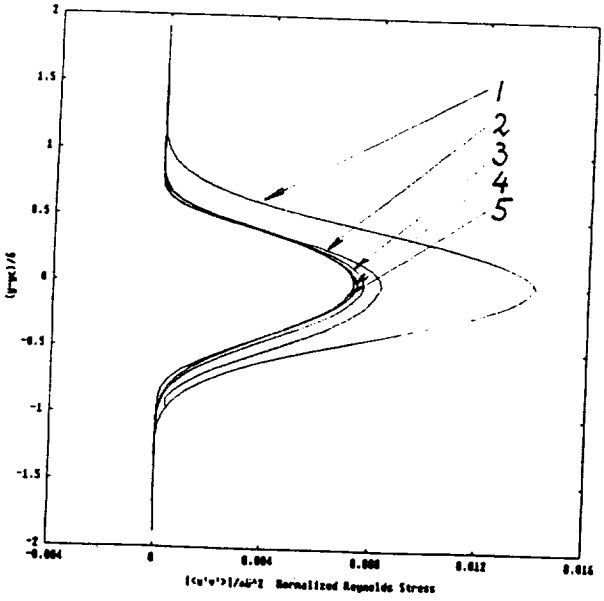

Fig. 12: Comparison of Reynolds stresses with five different convective Mach numbers.

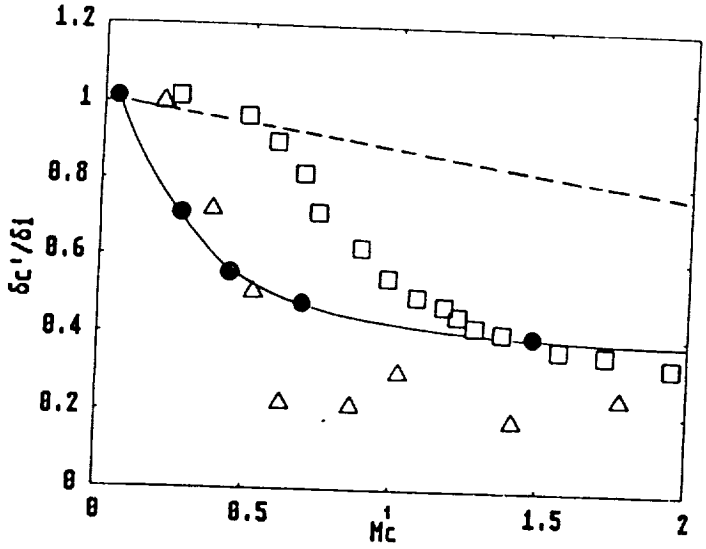

Papamoschou and Roshko [9]

Langley's data [7]

With Compressibility Model

Without Compressibility Model

Fig. 13: Comparison of ratios of spreading rate between experimental data and predicted results.